Y_2O_3:Eu micronic particles synthesised by spray pyrolysis: Global modelling and optimisation of the evaporation stage

N. Reuge [a], J. Dexpert-Ghys [b], M. Verelst [b], B. Caussat [a,*]

[a] *Laboratoire de Génie Chimique/ENSIACET/INPT, UMR CNRS 5503, 5 rue Paulin Talabot, BP1301, 31106 Toulouse Cedex 1, France*
[b] *CEMES, UPR CNRS 8011, 29 rue Jeanne Marvig, 31055 Toulouse Cedex, France*

Abstract

There are a number of some major advantages to be gained in processing micronic europium-doped yttrium oxide Y_2O_3 particles for phosphor applications using spray pyrolysis. In order to maximise production rates, it is tempting to use relatively dense sprays, but then coalescence occurs increasing final particle diameters, which must be prevented. Moreover, the influence of the operating conditions on the process behaviour is poorly understood. A complete one-dimensional model of the evaporation stage of micronic water/$Y(NO_3)_3$ droplets considering only the evaporation process and then both evaporation and gravity-induced coalescence phenomena has been established. Calculations of pure evaporation have shown that the amounts of evaporated water and droplet compositions depend only on the local temperature and not on the thermal history of the spray. Coupled calculations have shown that, in comparison with evaporation, coalescence plays a minor role on droplet diameter, but non-negligible as the increase of the final mean droplet diameter due to coalescence reaches up to 10% at low flow rates in the operating conditions tested. Injecting a preheated air flow directly into the nebuliser is a promising method to minimise coalescence effects: optimal operating conditions for which coalescence is completely insignificant were obtained by simulation.

Keywords: Spray pyrolysis; Evaporation; Coalescence; Modelling; Micronic particles; Yttrium nitrate

1. Introduction

Spray pyrolysis (SP) is an aerosol process commonly used to form a wide variety of materials in powder form [1,2] including metals, metal oxides, ceramics, superconductors, fullerenes and nanostructured materials. The sizes of the processed particles are most often micronic and sub-micronic (50 nm–5 μm). This technology has been used for many years in the material, chemical and food industries. It consists of five main steps: (i) generation of a spray from a liquid precursor by an appropriate droplet generator, (ii) spray transport by an air flow during which solvent evaporation occurs then concomitant solute precipitation when the solubility limit is exceeded inside droplets, (iii) thermolysis of the precipitated particles at higher temperatures to form micro/nano-porous particles, (iv) intra-particulate sintering to form dense particles and (v) finally, extraction of the particles from the gas flow. SP offers specific advantages over conventional material processing techniques [1,2] (gas-to-particle conversion processes, liquid or solid-state processing followed by milling), such as a higher purity of the produced powders, a better uniformity in chemical composition, a narrower size distribution, a better regularity in shape and the synthesis of multicomponent materials. Another advantage is the relative simplicity of the process which allows easy scale-up [3]. However, challenges still exist for SP, e.g. to increase production rates, to better understand the influence of the operating conditions to control particle size, shape and internal morphology (filled or hollow particles).

Europium-doped yttrium oxide (Y_2O_3:Eu) discovered decades ago, is still considered to be one of the best red inorganic phosphors, due to the sharp emission ($\lambda = 611$ nm) of the europium ion activator (Eu^{3+}) in the host lattice (Y_2O_3), its excellent luminescence efficiency, colour purity and stability [4]. SP is a promising alternative process for its large-scale production [3,5]. Y_2O_3:Eu micronic particles synthesised by SP from

* Corresponding author. Tel.: +33 5 34615211; fax: +33 5 34615253.
E-mail addresses: reuge@free.fr (N. Reuge), Brigitte.Caussat@ensiacet.fr (B. Caussat).

yttrium nitrate solutions are hollow spheres: we have shown [6] that the origin of this morphology was in the thermolysis step and not in the evaporation step. Indeed, the analysis of the phenomena occurring during the thermolysis step between 95 and 300 °C has revealed that a partial liquefaction of the hydrated yttrium nitrate occurs with concomitant release of gaseous water and N_2O_5. As a consequence, a crust of lightly hydrated yttrium nitrate probably appears, followed by particle inflation, leading to the formation of hollow spheres.

However, the study of the evaporation stage remains important to be able to increase production rates and to reduce coalescence phenomena. The general aim of the present work was therefore to determine the main parameters controlling this stage, including heat and mass transfer and coalescence phenomena, and to establish guidelines allowing its global optimisation.

Most of the modelling studies in the literature on this topic use 1D numerical approaches [7–10]. As it will be shown in this paper, this kind of model is often sufficient to describe the main phenomena occurring in this process and offers valuable information for its optimisation. However, few studies on sprays deal with both evaporation and coalescence phenomena [11–14], and only for applications in which the description of the evaporation process is quite simple (i.e. evaporation rates not affected by the presence of solutes). This can be explained by two main reasons: first, most of the previous works on SP were carried out in processing conditions in which no coalescence occurred. But scaling this process for significant production rates implies using denser sprays, so the problem of coalescence appears. Second, this is a very complex problem.

Two kinds of numerical approaches exist to simulate coalescence phenomena in droplet or bubble sprays: the first one is based on a physical description and the second one on a stochastic description. The former is the most rigorous approach but can hardly be used to model coalescence phenomena when droplet trajectories are multidimensional. The latter uses either the stochastic algorithm of O'Rourke and Bracco [15] (or an improved algorithm based on it) and requires a 2D (or 3D) Euler–Lagrange unsteady frame or the multifluid Eulerian model introduced by Tambour and co-workers [16]. Although stochastic approaches can be very efficient to model complex coalescence phenomena in relatively small areas [11,17], they are quite time-consuming and thus not really well suited for so long geometrical domains such as drying columns.

A pilot-scale SP set-up has been assembled in our group and tested with water solutions of yttrium nitrate. The very high cost of europium imposed the use of pure yttrium nitrate for the experiments, as large amounts of particles were needed. Since the thermo-chemical properties of Y and Eu are very close and moreover the molar doping level in the red phosphor is low (1Eu/19Y), we can safely assume that the results of experiments and modelling for SP from pure yttrium nitrate are also valid for the red phosphor precursor.

In order to optimise the process, a 1D modelling study was performed and the influence of the main operating parameters numerically studied. Firstly, only evaporation was considered. Solute concentrations and temperatures were assumed to be uniform inside the droplets: these assumptions are easily justified estimating the characteristic times of mass and heat diffusion [7,10]. Gas and liquid temperatures, droplet diameters and solute concentrations inside droplets were calculated along the column axis for various processing conditions.

Secondly, coalescence was also taken into account. The configuration of our experimental set-up (i.e. a vertical drying column) and the nature of the coalescence phenomena involved (i.e. gravity-induced coalescence) allowed to develop a 1D numerical approach based on physical models. Calculated droplet diameters were compared to experimental data and the respective influences of coalescence and evaporation on the droplet size evolution were analysed. Finally, methods are proposed to minimise final droplet diameter.

2. Process description and operating conditions

An ultrasonic generator (ARECO/ARIV) working at 1.6 MHz formed micronic droplets from $Y(NO_3)_3$ diluted in water at 0.6 mol l^{-1}. The droplets were transported by an air flow through successively:

- a vertical drying column: 20 cm internal diameter, 1.8 m long;
- then a horizontal decomposition/densification column: 20 cm internal diameter, 1.8 m long.

The heating system was composed of juxtaposed electrical furnaces of 12 kW of total power. Thermocouples are put on the outer wall of the reactor and allowed the temperature to be adjusted up to 250 °C in the drying zone and up to 1000 °C in the decomposition/densification zone. The solid phase was then separated from the vapour phase by a bag filter.

For the experiments described here, the inlet spray temperature was equal to 31 °C, and the outer wall temperature of the drying zone was fixed at 225 °C. Four air flow rates were considered: 2, 3.5, 5 and 8.2 $m^3\,h^{-1}$ STP. The flow rates of the nebulised solution depended on the configuration of the apparatus:

- When the flow escapes freely out of the column in the absence of filter (i.e. open configuration), the flow rates of solution are given by the following law:

$$Fv_{liq} = 2.2 \times 10^{-4} Fv_a \qquad \text{(law 1)}$$

  which gave rise to solution flow rates equal to 0.44, 0.77, 1.1 and 1.8 l h^{-1} STP, respectively.
- In fully operational conditions, a bag filter is put at the outlet of the pyrolysis column (i.e. closed configuration), a slight overpressure appears in the whole apparatus resulting in lower flow rates of solution, given by:

$$Fv_{liq} = 1.17 \times 10^{-4} Fv_a \qquad \text{(law 2)}$$

  which led to solution flow rates of: 0.23, 0.41, 0.58 and 0.96 l h^{-1} STP, respectively. Note that pure water sprays were also generated in the same operating conditions for the needs

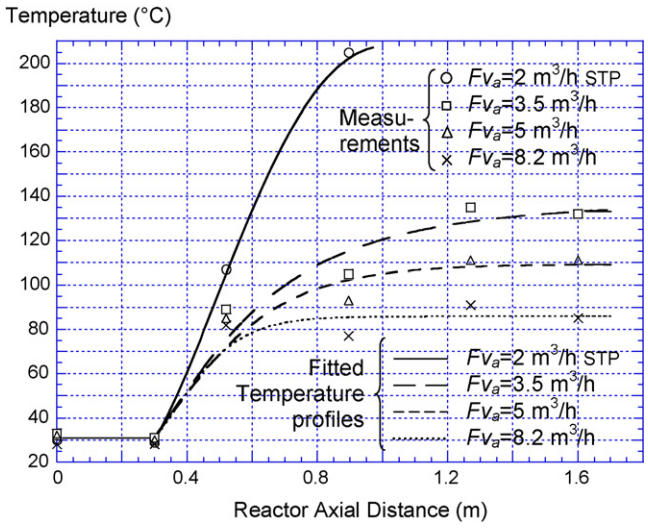

Fig. 1. Inner wall temperatures measured along the reactor axis for several air flow rates/pure water flow rates following law 1—fitted temperature profiles used for calculations.

of the modelling study. Laws 1 and 2 are also valid for pure water.

Droplet diameter distributions have been measured with a Spraytech^{TM} Malvern laser size analyser positioned at the entrance and at the exit of the drying column, at the half-radius. Measurements have been first performed on a cold spray of the solution, and then, some attempts have been made at the column exit with the heating activated, but these latter measurements could unfortunately not be used for this study because we noticed that the temperature of the spray was significantly altered by the presence of the granulometer.

The droplet volume mean diameters measured at the column inlet were, respectively, of 5.4, 5.3, 5.2 and 5.9 μm in the order of increasing air flow rates, giving around 1.4×10^6 droplets cm^{-3}.

As presented in Fig. 1, inner wall temperatures have been measured along the column height for the four air flow rates tested and for sprays of pure water following law 1 (i.e. open configuration). It appears that the first 30 cm of the column are not heated by the furnaces. Then, temperatures increase along the column height and finally tend to reach a plateau. Logically, the higher is the air/water flow rate, the lower are the wall temperatures along the reactor height.

Finally, it must be emphasised that preliminary calculations showed that, over the whole range of operating parameters, evaporation was extremely intense at ambient temperature as long as the air was not completely saturated with water vapour at the droplet surface (i.e. an interfacial relative humidity of 100%). Since this fast evaporation occurred between the nebulisation area and the reactor inlet, the air at the droplet surface was already completely saturated with water vapour at the reactor inlet and the solute concentration inside the droplets was no longer 0.6 mol l^{-1}, but 0.75 mol l^{-1}. The inlet value of the specific humidity of air Y_0 was therefore 0.026.

3. 1D model of evaporation

3.1. Assumptions, equations and physical properties of the fluids

A model which is 1D at the column scale and 0D at the droplet scale was developed first. The following assumptions were made:

(i) Gas flow is laminar since the Reynolds number varies between 200 and 1000.

(ii) All parameters are uniform inside the droplets: in our range of operating parameters, the ratio (R_1) of the characteristic time of diffusion for solute diffusion in a droplet [7,18,19] to the total time of evaporation remains lower than 5×10^{-4}, which is very weak, meaning that solute concentration gradients can a priori be ignored. Note that some accurate calculations performed using a precise 1D spherical model, by considering convection and a precise description of diffusion, have confirmed that concentration gradients can be ignored [6]. Xiong and Kodas [10] came to the same conclusion for similar processing conditions. Likewise, we estimated the ratio (R_2) of the characteristic time for heat diffusion in the droplet [7,10,19] to the total time of evaporation: this ratio is lower than R_1 by several orders of magnitude. The assumption of uniform temperature in droplets is therefore fully justified.

(iii) At the column scale, momentum, heat and mass transfer phenomena in the radial direction were ignored. This assumption is justified since measurements showed that the mean radial temperature gradient was 3.5 °C cm^{-1} and only 1.2 °C cm^{-1} between a radial position of 2.5 cm from the wall and the centre of the column. 2D axisymmetric calculations were performed and showed that radial heat diffusion was mainly due to radiation between droplets and reactor walls.

(iv) The heat flux density q brought from the furnaces to the spray through the column walls is proportional to the difference between the inner wall and spray temperatures:

$$q = \kappa(T_{\text{wall}} - T_{\text{spray}}) \quad (1)$$

The spray temperature T_{spray} can be defined as an average between gas and droplets temperatures (balanced by their respective flow rates). But these two temperatures were always equal over our whole range of processing conditions as evidenced by calculation. The value of the overall heat transfer coefficient κ was adjusted for each air flow rate such that the temperatures calculated fit the mean temperatures measured in the droplets/air fluxes along the column, for sprays of pure water and for the open configuration. The same values of κ and the associated temperature profiles were used for the whole study whatever the spray nature (pure water or water/$Y(NO_3)_3$) and the configuration of the column (open or closed).

(v) The relative velocity between droplets and carrier gas is zero and there is no interaction between droplets.

(vi) Axial diffusion of water vapour in air is negligible.
(vii) The Kelvin effect is negligible because droplets remain much larger than 0.1 μm [19].
(viii) The solute begins to precipitate as soon as the saturation concentration is reached, supersaturation concentration of yttrium nitrate in water being unknown.

The mean mass fractions of water inside droplets/particles and in air are given by the following dimensionless expressions:

$$\begin{cases} X = w_{\mathrm{w}}^{\mathrm{liq}} (w_{\mathrm{s}}^{\mathrm{liq}})^{-1} \\ Y = w_{\mathrm{w}}^{\mathrm{vap}} w_{\mathrm{a}}^{-1} \end{cases} \tag{2}$$

Four equations must be solved: that of mass conservation at the reactor scale (3) and at the droplet scale (4), the energy equation at the reactor scale (5) and at the droplet scale (6). Considering the assumptions previously detailed, they take the following form:

$$F_{\mathrm{a}} Y + F_{\mathrm{s}} X = F_{\mathrm{w}} \tag{3}$$

$$v_{\mathrm{gas}} m_{\mathrm{s}} \frac{\partial X}{\partial z} = -(4\pi R) D_{\mathrm{v}} \rho_{\mathrm{a}} \left(Y_{\mathrm{int}} \left(\frac{T_{\mathrm{gas}}}{T_{\mathrm{liq}}} \right) - Y \right) \tag{4}$$

$$F_{\mathrm{s}}(1+X)\, Cp_{\mathrm{d}} \frac{\partial T_{\mathrm{liq}}}{\partial z} + F_{\mathrm{a}}(Cp_{\mathrm{a}} + Y\, Cp_{\mathrm{w}}^{\mathrm{vap}}) \frac{\partial T_{\mathrm{gas}}}{\partial z} - F_{\mathrm{s}} h_{\mathrm{vap}} \frac{\partial X}{\partial z} - \frac{\partial}{\partial z} \left(\lambda_{\mathrm{gas}} \frac{\partial T_{\mathrm{gas}}}{\partial z} \right) (\pi R_{\mathrm{c}}^2) = q(2\pi R_{\mathrm{c}}) \tag{5}$$

$$v_{\mathrm{gas}} m_{\mathrm{d}}\, Cp_{\mathrm{d}} \frac{\partial T_{\mathrm{liq}}}{\partial z} = (4\pi R) \lambda_{\mathrm{gas}} (T_{\mathrm{gas}} - T_{\mathrm{liq}}) + v_z m_{\mathrm{s}} h_{\mathrm{vap}} \frac{\partial X}{\partial z} \tag{6}$$

where air, water and solute flow rates F_{a}, F_{w} and F_{s} are expressed in kg s^{-1}. The main physical properties of the fluids are given in Table 1 [20–23]. Note that these equations have been successfully validated by Yu and Liao [9] from experimental investigations of evaporation of water/NaCl and water/NH_4NO_3 droplets performed by Ranz and Marshall [24].

The reduced mass fraction of water Y_{int} at the liquid/gas interface at the saturation pressure is defined as:

$$Y_{\mathrm{int}} = a_{\mathrm{w}} M_{\mathrm{w}} (M_{\mathrm{a}} P_0)^{-1} P_{\mathrm{sat}} \tag{7}$$

where a_{w} is the water activity, dependent on X, P_0 the total pressure at the column inlet and P_{sat} is the water vapour saturation pressure in air.

The droplet mass can be written as:

$$m_{\mathrm{d}} = m_{\mathrm{s}}(1+X) = \rho_{\mathrm{liq}} \left(\tfrac{4}{3} \right) \pi R^3 \tag{8}$$

where m_{s} is the mass of solute in a droplet, ρ_{liq} the droplet density and R is its radius. From the latter equation, the following expression for the droplet radius can be deduced:

$$R = R_0 \left(\frac{\rho_{\mathrm{liq},0}}{\rho_{\mathrm{liq}}} \frac{1+X}{1+X_0} \right)^{1/3} \tag{9}$$

where R_0, X_0 and $\rho_{\mathrm{liq},0}$ are the initial values of R, X and ρ_{liq}. The expression of the droplet radius R_{p} at the onset of precipitation is given by:

$$R_{\mathrm{p}} = R_0 \left(\frac{\rho_{\mathrm{liq},0}}{\rho_{\mathrm{liq}}^{\mathrm{sat}}} \frac{1+X_{\mathrm{sat}}}{1+X_0} \right)^{1/3} \tag{10}$$

where X_{sat} and $\rho_{\mathrm{liq}}^{\mathrm{sat}}$ are, respectively, the values of X and the droplet density at the solubility limit.

Depending on the droplet temperature at the onset of precipitation, note that the precipitate actually formed can be $Y(NO_3)_3{\cdot}6H_2O$ or $Y(NO_3)_3{\cdot}5H_2O$ [23].

We also used this system of equations to calculate the evaporation of a pure water spray taking a small solute mass flow rate F_{s} (10^{-12} kg s^{-1}), a droplet density equal to the water density ρ_{w} and a water activity equal to 1.

All these equations were implemented in the finite element solver FlexPDE [25], which uses a modified Newton–Raphson iteration process and a mesh generator with automatic refinement. The code implemented in FlexPDE was numerically validated using the results of Yu and Liao [9] as a basis and by calculations performed with the ODE solver Scilab [26] over the whole range of our operating conditions.

3.2. Results and discussion

Spray temperatures were measured in four radial positions and in six axial positions along the reactor for each flow rate studied in the open configuration. Radial average values were considered; these and the calculated ones are reported

Table 1
Physical properties of water and aqueous $Y(NO_3)_3$

Density (kg m^{-3}), from [20]
ρ_{liq} (25 °C) $= a_1 + a_2/X + a_3/X^{1.5} + a_4/X^2 + a_5/X^{2.5} + a_6/X^3 + a_7/X^{3.5} + a_8/X^4 + a_9/X^{4.5}$, with: $a_1 = 995$; $a_2 = 0.8178$; $a_3 = 2.855 \times 10^{-2}$; $a_4 = -0.8367$; $a_5 = 2.2764$; $a_6 = -4.1271$; $a_7 = 3.9393$; $a_8 = -1.8699$; $a_9 = 0.3532$

Water activity, from [20]
a_{w} (25 °C) $= \exp[(-4/X)(18/275)(1 - (b_0/X^{0.5}) + (b_1/X^{0.75}) + (b_2/X) + (b_3/X^{1.25}) + (b_4/X^{1.75}) + (b_6/X^2) + (b_7/X^{2.25}))]$, with: $b_0 = 5.4939$; $b_1 = -7.8834$; $b_2 = 164.4546$; $b_3 = -555.8051$; $b_4 = 913.9005$; $b_5 = -814.9047$; $b_6 = 378.477$; $b_7 = -71.97$

Water vapour saturation pressure in air (Pa), from [21]
$P_{\mathrm{sat}} = (10^5/760) \exp(18.3036 - (3816.44/(T_{\mathrm{liq}} - 46.13)))$

Solubility (g/100 g of water) fitted from experimental results [22,23]
$S = c_0 + c_1 T_{\mathrm{liq}} + c_2 \arctan(c_3 T_{\mathrm{liq}} - c_4)$, with: $c_0 = -150.3776$; $c_1 = 1.1185$ K^{-1}; $c_2 = 25.3241$; $c_3 = 0.1588$ K^{-1}; $c_4 = 54.5378$

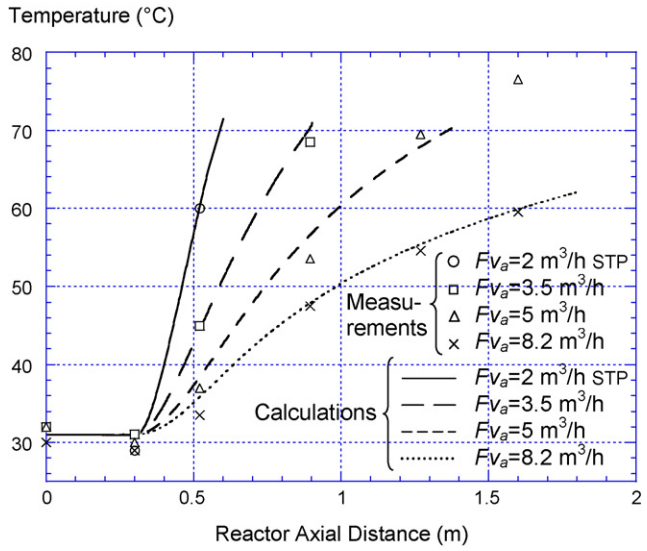

Fig. 2. Average spray temperatures measured along the reactor axis for several air flow rates/pure water flow rates following law 1 compared to the calculated spray temperatures.

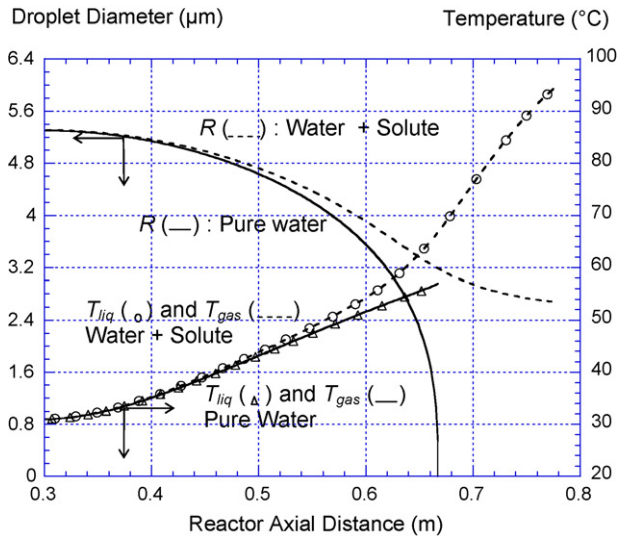

Fig. 3. Variation of the droplet diameter, gas and liquid temperatures along the reactor axis for pure water and water + $Y(NO_3)_3$—$Fv_a = 3.5\ m^3\ h^{-1}$ STP, $Fv_w = 0.411\ h^{-1}$ STP, $d_0 = 5.3\ \mu m$.

in Fig. 2. A good agreement was obtained using the following values of κ in order of increasing flow rates: 55, 42, 28 and $27\ W\ m^{-2}\ K^{-1}$. This variation of κ is difficult to interpret: as specified by Bird et al. [27], the overall heat transfer coefficient depends in a complicated way on many variables, including the fluid properties, the flow velocity, the value of the characteristic temperature difference and the temperature distribution.

For a given position in the column, the spray temperature decreases if the flow rate increases. Calculations were stopped at the onset of precipitation, which always occurs at a temperature of about 71 °C for these processing conditions.

Then, calculations were carried out again considering the column in the closed configuration (i.e. solution flow rates following law 2).

First, the evaporation stage was studied for an air flow rate of $3.5\ m^3\ h^{-1}$ STP. Fig. 3 presents the evolution of the droplet diameter and of gas and liquid temperatures calculated along the reactor axis for pure water and water/$Y(NO_3)_3$ solutions. It can be observed that the decrease of the radius of pure water droplets is faster than the decrease of the radius of water + solute droplets: evaporation is complete at a position of 0.66 m for pure water droplets whereas the solubility limit is reached at 0.78 m for water + solute droplets. This is due to the fact that in the latter case, the lower water activity involves a lower interfacial saturation pressure and therefore a lower evaporation rate. It can be deduced that the water of the solution requires a higher energy to be vapourised, about 18% more in the operating conditions tested.

For both pure water and $Y(NO_3)_3$ solutions, the temperature of the liquid phase remains always equal to that of the gas phase as reported in Fig. 3. This result is due to the high value of the heat transfer coefficient at the liquid/gas interface. Evaporation of pure water droplets is complete at 56 °C whereas water + solute droplets reach the onset of precipitation at 95 °C.

Fig. 4 presents the temporal evolution of $(R/R_0)^2$ for pure water and water + solute droplets at the four air flow rates in the closed configuration. It can be observed that once the spray enters the hot zone, evaporation occurs and droplet diameters follow roughly the so-called D^2-law (i.e. the variation of droplet surface area *vs*. residence time is linear) [24,28]. For the three lowest air/solution flow rates, the onset of precipitation is always reached for a ratio R/R_0 equal to 0.5, a solute concentration of $5.9\ mol\ l^{-1}$ and a droplet temperature equal to 95 °C. Thus, final droplet diameters (R_p is given by (10)) are of 2.7, 2.65 and 2.6 µm, after 30, 24 and 23.5 s of evaporation, respectively, in the order of increasing air flow rates. However, for the highest air/solution flow rate, the onset of precipitation is never reached and the droplet diameter stabilises at a value of 3.1 µm towards

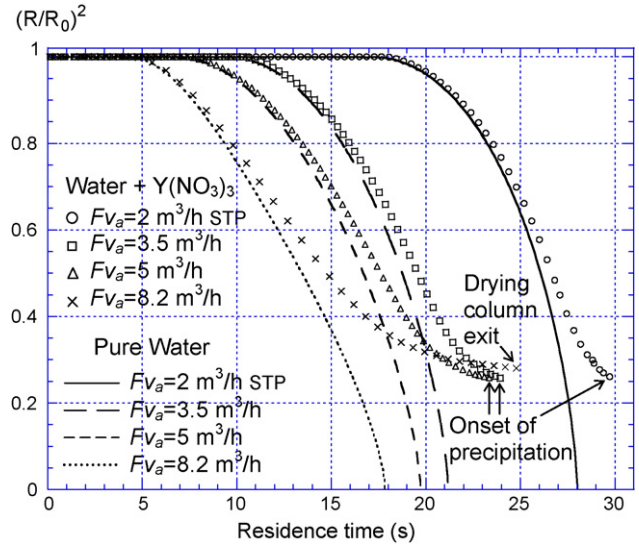

Fig. 4. Variation of $(R/R_0)^2$ vs. residence time for pure water and water + $Y(NO_3)_3$, for several air flow rates/solution flow rates following law 2.

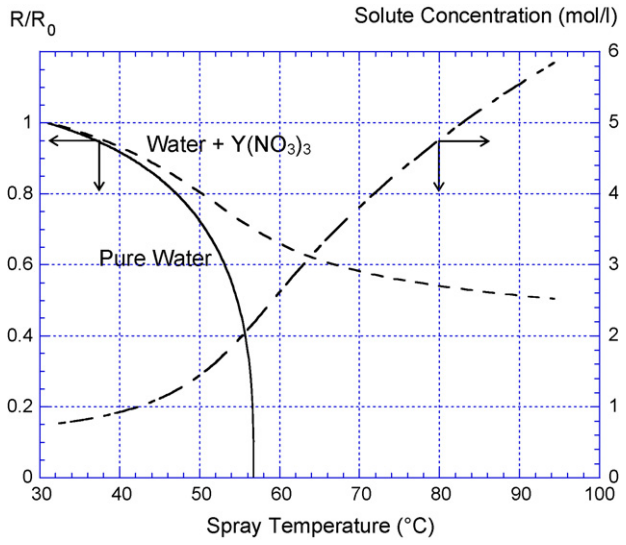

Fig. 5. Variation of the dimensionless droplet radius for pure water and water + $Y(NO_3)_3$ and of the solute concentration vs. spray temperature.

the end of the drying column. This is due to the fact that for these operating conditions the inner wall temperature does not exceed 86 °C as can be seen in Fig. 1 and therefore the spray cannot be heated to 95 °C.

Moreover, calculations showed that the reactor height necessary for a complete evaporation increases with the air/water flow rate. Actually, the total energy consumed during the evaporation stage is proportional to the air/solution flow rate and is equal to about 2520 kJ l^{-1} of solution for the evaporation stage (i.e. a total power of 700 W).

The variations of the dimensionless droplet radius and of the solute concentration into droplets versus spray temperature are reported in Fig. 5: they are the same whatever the initial flow rates in the range studied. This can be explained by the fact that the limiting step here is clearly heat transfer from reactor walls to the spray, not mass transfer at the air/water interface and/or inside the droplet. Actually, at a given position in the reactor, the local temperature determines the interfacial saturation pressure and therefore the total amount of evaporated water. It can be deduced that the droplet radius and the solute concentration depends only on the local temperature and not on the thermal history of the spray. This result is verified for a wide range around our operating parameters, and it remains valid for heat flux densities up to 10 times higher and spray densities up to 10 times lower.

3.3. Evolution of droplet size distribution

Before studying the effect of coalescence, it is necessary to apply the 1D model of pure evaporation of Section 3.1 considering an initial distribution of droplet sizes.

In the case of a spray of pure water, Eq. (4) can be written as:

$$\rho_w \frac{\partial R^3}{\partial t} = -4\pi R D_v \rho_a \Delta Y \tag{11}$$

Then, let us consider two populations of droplets of different initial radii R_{i0} and R_{j0} with $R_{i0} < R_{j0}$. From Eq. (11), we can write:

$$\frac{dR_i/dt}{dR_j/dt} = \frac{R_j}{R_i} \tag{12}$$

Therefore, small droplets evaporate faster than larger ones and we can deduce the following relation:

$$R_{j0}^2 - R_j^2 = R_{i0}^2 - R_i^2 \tag{13}$$

which is valid as long as the smallest droplets have not completely evaporated. However, as mentioned in the previous part, note that the total amount of evaporated water still depends only on the local temperature for the operating conditions tested.

In the case of a spray of water + solute, we can write:

$$\frac{d(\rho_{liq} R_i^3)/dt}{d(\rho_{liq} R_j^3)/dt} = \frac{R_i}{R_j} \frac{a_{w_i} P_{sat} - P_{vap}}{a_{w_j} P_{sat} - P_{vap}} \tag{14}$$

where a_{w_i} and a_{w_j} are the water activities in the droplets of radius R_i and R_j, and P_{vap} is the partial pressure of water vapour in air. No direct interpretation can be deduced from this relation because water activities (dependent on solute concentrations) act on the evaporation rate in an opposite way of the radius.

Consequently, it was necessary to perform complete calculations of the evaporation of water + $Y(NO_3)_3$ droplets with different initial radii: the equation of mass conservation at the droplet scale (4) was implemented three times for three populations of droplets of different initial radii (in the range 1.5–4 μm). As a result, we found that the temporal decrease of radius (i.e. $d(R_i/R_{i0})/dt$) is the same whatever the droplet radius.

Since the total amount of evaporated water still only depends on the local temperature, we can write the following relation whatever the initial droplet radius:

$$\frac{R_i}{R_{i0}} = f(T) \tag{15}$$

where f is a function which can be determined by 1D calculations. Moreover, this result implies that the compositions of all the droplets are the same at a given height in the column and that R_i/R_{i0} still follows the evolution shown in Fig. 5.

With processing conditions involving much more rapid heating, in which the limiting step is the evaporation and not the heat transfer from reactor walls to the spray, relation (15) is of course no longer valid: calculations show that the evaporation of the different populations of water + solute droplets occurs in the same way as for pure water and droplet radii follow relation (13).

4. 1D model of coalescence and evaporation

4.1. 1D model of coalescence

Coalescence of droplets in a spray can have various origins. The commonly encountered causes of coalescence are the following [19,29]:

- Brownian motion,
- gravitational motion,
- shear flow,
- turbulence,
- thermophoresis.

For our operating conditions, coalescence induced by Brownian motion (or thermal coagulation) is insignificant because the droplet concentration number (2.35×10^6 cm^{-3}) is too low: for typical residence times considered in this study (i.e. a few tens of seconds), thermal coagulation would become important for sprays about 100 times denser [19,29]. The flow is laminar in the drying column, so coalescence cannot be induced by turbulence. However, Reynolds numbers may be very high in the droplet generator and there, coalescence due to turbulence can be significant. Then, except perhaps in the immediate vicinity of the walls of the drying column, radial gradients of droplet velocities and of temperature are too small by several orders of magnitude for coalescence to be induced by shear flow or thermophoresis [30,31]. Therefore, only the gravity-induced coalescence remains.

As a consequence, the droplets introduced into the drying column mainly undergo the gravity and the drag forces of the carrier gas. The drag forces depend on droplet mass and diameter. Thus, small droplets travel more quickly than bigger ones and as a result coalescence occurs. In this part, we will consider undeformed spherical droplets of same density ρ_{liq} and will assume that no evaporation occurs.

Consider a spray composed of two populations of droplets i and j, of different radii: $R_j > R_i$ and therefore different velocities: $v_i > v_j$. The carrier gas rises vertically in the drying column along $\mathbf{e}_z$ axis at the velocity v_{gas}. The coalescence frequency of droplets i with a droplet j can be written [29,32–34] as:

$$f_{ij} = \pi(R_i + R_j)^2 n_i (v_i - v_j)\varepsilon_{ij} \tag{16}$$

where n_i is the number density of droplets i and ε_{ij} is the coalescence efficiency (i.e. the probability that two neighbouring droplets of different sizes moving initially on the same trajectory collide effectively multiplied by the probability that these two colliding droplets coalesce effectively).

Then, the coalescence frequency of droplets i with droplets j can be written as:

$$F_{ij} = \pi(R_i + R_j)^2 n_i n_j (v_i - v_j)\varepsilon_{ij} \tag{17}$$

During an infinitesimal time dt, the carrier gas achieves a distance dz equal to $v_{\text{gas}}\,\mathrm{d}t$. A time equal to $v_{\text{gas}} v_j^{-1}\,\mathrm{d}t$ is required for droplets j to accomplish the same distance dz. Therefore, the variation of the number density of droplets i along dz can be written as:

$$\frac{\mathrm{d}n_i}{\mathrm{d}t} = -F_{ij}\frac{v_{\text{gas}}}{v_j} \tag{18}$$

Following a similar reasoning about droplet volumes, we can write:

$$\frac{\mathrm{d}R_j^3}{\mathrm{d}t} = f_{ij}\frac{v_{\text{gas}}}{v_j}R_i^3 \tag{19}$$

Then, it is possible to generalise Eqs. (18) and (19) to a spray composed of n populations of droplets with different radii (with: $R_n > R_{n-1} > \cdots > R_j > \cdots > R_i > \cdots > R_1$):

$$\frac{\mathrm{d}n_i}{\mathrm{d}t} = -\sum_{j=i+1}^{n} F_{ij}\frac{v_{\text{gas}}}{v_j} \tag{20}$$

$$\frac{\mathrm{d}R_i^3}{\mathrm{d}t} = \frac{v_{\text{gas}}}{v_i}\sum_{j=1}^{i-1} f_{ji} R_j^3 \tag{21}$$

Droplet velocities are calculated using the equation of momentum conservation [27]. For a droplet j, this equation is given by:

$$\frac{\mathrm{d}\mathbf{p}_j}{\mathrm{d}t} = \mathbf{F}_{\mathrm{D},j} + \mathbf{F}_{i\to j} + \mathbf{P}_j \tag{22}$$

where $\mathbf{F}_{\mathrm{D},j}$ is the drag force applied by the carrier gas on the droplet j, $\mathbf{F}_{i\to j}$ the force resulting from the transmission of momentum from droplets i to a droplet j and $\mathbf{P}_j$ is the gravity force.

First, we took the transmission of momentum into account in the model (see Appendix A for further developments), but calculations revealed it to be negligible for our operating conditions. Considering only the drag and gravity forces, and assuming that the droplet has reached a constant velocity (actually done after few tenths of seconds for our droplet diameters, see [19]), Eq. (22) becomes:

$$v_j = v_{\text{gas}} - \sqrt{\frac{8}{3}\frac{\rho_{\text{liq}}}{\rho_{\text{gas}}}\frac{R_j}{C_{\mathrm{D},j}}g} \tag{23}$$

where $C_{\mathrm{D},j}$ is the drag force coefficient (see Appendix A).

The second term of relation (23) is the so-called terminal settling velocity [19,29] of the droplet j. Since $C_{\mathrm{D},j}$ depends on v_j by quite a complex relation, v_j cannot be determined analytically, so preliminary calculations are needed (see (A.13)).

Thus, Eqs. (20) and (21) provide a consistent system of $2n$ equations and $2n$ variables allowing the 1D problem of coalescence to be solved.

4.2. Coupling of coalescence and evaporation

We will only consider the case of a spray composed of water + solute droplets. If coalescence occurs, relation (15) is no longer strictly valid, but, between two collisions, each individual droplet continues to follow it. Thus, the evaporation process is still controlled by the local temperature and compositions and densities of all droplets remain locally equal. Actually, considering the effect of coalescence, relation (15) is still valid if R_{i0} is replaced by a virtual radius $R_{i0}^{\dagger}$ taking into account the coalescence process:

$$\frac{\mathrm{d}R_{i0}^{\dagger 3}}{\mathrm{d}t} = \frac{v_{\text{gas}}}{v_i}\sum_{j=1}^{i-1} f_{ji} R_{j0}^{\dagger 3} \tag{24}$$

Then, we can write:

$$\frac{\mathrm{d}R_i^3}{\mathrm{d}t} = \frac{\mathrm{d}}{\mathrm{d}t}(R_{i0}^{\dagger 3} f^3(T)) = R_{i0}^{\dagger 3} \frac{\partial f^3}{\partial T} \frac{\mathrm{d}T}{\mathrm{d}t} + f^3(T) \frac{v_{\mathrm{gas}}}{v_i} \sum_{j=1}^{i-1} f_{ji} R_{j0}^{\dagger 3} \tag{25}$$

Eq. (20) remains unchanged. Then, the numerical scheme to solve the coupled problem is the following:

- The 1D problem of pure evaporation is solved first with a unique droplet radius (the mean size of the distribution, for instance). This gives the function $f(T)$ and $\mathrm{d}T/\mathrm{d}t$.
- Eqs. (20) and (25) are solved by taking the previously calculated function $f(T)$ into account. Of course, the calculation is stopped at the onset of precipitation.

It is important to note that such a scheme is usable because the total evaporation rate does not depend on the coalescence process.

Coalescence equations were implemented in the ODE solver Scilab [26]. Regarding the high number and the complexity of equations (21 equations and 21 variables in the heaviest case), a Fortran program was first written to generate the source files directly usable by Scilab. Time steps of 1 ms were used.

4.3. Results and discussion

First, it must be emphasised that the following results depend on the precision of the measurements. Uncertainties on measured droplet diameters are not directly imputable to the granulometric measurements themselves (accuracy: ±1%) but rather due to difficultly avoidable variations of operating conditions in such a large experimental set-up and to the sensitivity of the coalescence process to these variations. Uncertainties on mean volume droplet diameters measured can be estimated at ±5%.

4.3.1. Cold spray

In the case of an unheated spray, evaporation does not occur and only the coalescence process has to be modelled. Droplet size distributions measured at the entrance of the column in the open configuration were used as initial data for the calculations and measured droplet size distributions at the drying column exit were compared to the calculated ones. For instance, the volume distribution of the droplet diameters measured at the column entrance for the open configuration and an air flow rate of 3.5 $\mathrm{m^3\,h^{-1}}$ STP is reported in Table 2: droplet diameters vary in the range of 3.6–7.4 μm, the droplet volume mean diameter is equal to 5.3 μm and the standard deviation of the distribution to 0.55 μm. The volume distribution measured at the column exit for the same configuration and air flow rate is also presented in Table 2: droplet diameters now vary in the range of 4.3–8.8 μm, the droplet volume mean diameter is equal to 6.5 μm and the standard deviation to 0.7 μm. Thus, an increase of 23% of the mean diameter and of 27% of the standard deviation is observed.

Calculations could not be achieved for the lowest flow rate because the larger droplets reached the critical size for which the terminal settling velocity is equal to the gas velocity: this means that they necessarily finish by falling down, capturing yet more and more droplets throughout their fall. Such events cannot be taken into account by our model. Note that the effect of momentum transmission proved to be no longer negligible when droplets diameters were close to their critical value.

The coalescence efficiency was considered as constant, whatever the diameters of the colliding droplets, and was adjusted for the best agreement to be obtained between the calculated and the experimental results in terms of final droplets volume mean diameters. This was the case for a value of ε_{ij} equal to 0.39.

The volume distribution calculated at the column exit for the air flow rate of 3.5 $\mathrm{m^3\,h^{-1}}$ STP is reported in Table 2: droplet diameters vary in the range of 4.1–13 μm, the calculated droplet volume mean diameter of 6.6 μm is very close to the measured one whereas the standard deviation of the distribution of 1.7 μm is overestimated. Further calculations showed that uncertainties of ±10% on the values of the coalescence frequencies led to uncertainties lower than ±5% on the final droplet volume mean diameter and lower than ±15% on the final standard deviation. Therefore, reasonable changes of the values of the coalescence frequencies have a relatively limited effect on the results of our calculations.

Initial and final droplet volume mean diameters measured versus air flow rate are presented in Fig. 6. Initial diameters vary in the range of 5.2–5.8 μm, the maximum value being obtained for the highest flow rate. The standard deviation of the distributions varies slightly around 0.58 μm. Final droplet volume mean

Table 2
Volume droplet diameter distributions measured at the column inlet and at the column exit at the half radius and calculated at the column exit, for $\mathrm{Fv_a} = 3.5\ \mathrm{m^3\,h^{-1}}$ STP, $\mathrm{Fv_w} = 0.771\,\mathrm{h^{-1}}$ STP and a cold spray

Inlet: measurements		Exit: calculations		Exit: measurements	
Diameters (μm)	Volume fraction	Diameters (μm)	Volume fraction	Diameters (μm)	Volume fraction
3.21	0	–	–	3.25	0
3.61	5×10^{-4}	3.61	1.8×10^{-4}	3.74	10^{-4}
4.07	0.029	4.07	0.012	4.31	0.001
4.58	0.12	4.59	0.062	4.97	0.0063
5.16	0.54	5.26	0.39	5.75	0.33
5.81	0.23	6.77	0.31	6.58	0.45
6.54	0.076	9.38	0.22	7.61	0.21
7.37	5×10^{-4}	13.3	0.0029	8.77	0.0025
8.3	0	–	–	10.11	0

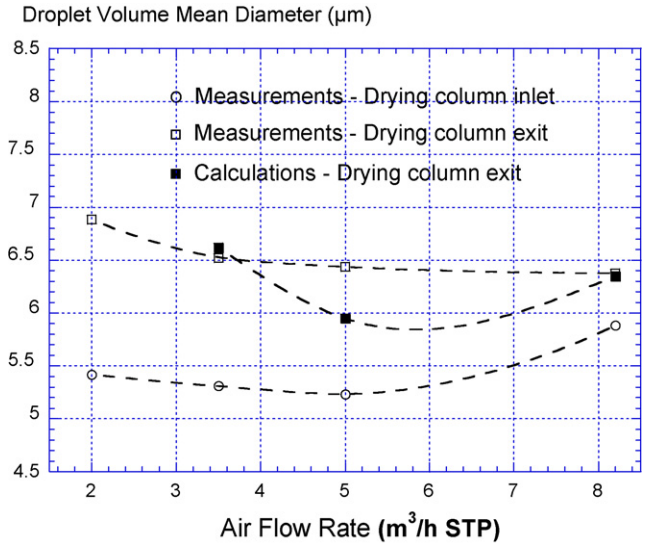

Fig. 6. Volume droplet mean diameters measured and calculated for several air flow rates/solution flow rates following law 1, cold spray.

diameters vary in the range of 6.4–6.9 µm, thus it has increased from 9.5% for the highest flow rate to 27% for the lowest flow rate. The standard deviation of the distributions varied in the range of 0.65–0.78 µm: it increased from 3% for the highest flow rate to 32% for the lowest flow rate. Therefore, the lower is the flow rate, the stronger the effect of coalescence. It was quite an expected result since the residence time of the spray in the column increases as the flow rate decreases.

Final droplet volume mean diameters calculated versus air flow rate are also presented in Fig. 6: they vary in the range of 5.95–6.6 µm and the standard deviation in the range of 0.97–1.7 µm with a minimum value for the highest flow rate. Thus, the agreement is also acceptable concerning the droplet volume mean diameter calculated for the highest flow rate, but it is less good for the intermediate flow rate: the droplet volume mean diameter calculated is underestimated by 7.5%. Calculated standard deviations were always overestimated.

As for the measurements, calculations show the effect of a coalescence decrease when the flow rate increases. A minimum final droplet diameter is found for the intermediate flow rate but this result is only due to the fact that a larger initial droplet mean diameter was measured for the highest flow rate.

A coalescence efficiency of 0.39 is higher than expected: from the theoretical investigations of Zhang and Davis [33,35], it should not exceed 0.1 for droplet diameters of about 1–10 µm. However, as mentioned by [29], the experimental investigations of Barbes Le Borgne [36] on bimodal aerosol of diameters of 1 µm/3 µm also led to coalescence efficiencies in the range of 0.3–0.4. Actually, the notion of coalescence efficiency covers extremely complex phenomena [37] which are not dealt with in our study. In particular, the presence of the dilute salt in the droplet could increase the coalescence efficiency modifying interparticle forces and droplet surface tensions.

It is also difficult to interpret the discrepancies between the standard deviations of the distributions calculated and of those measured. No conclusive argument has been found to explain it. A better discretisation of the initial distributions would probably not change the results significantly. However, taking a coalescence efficiency of 0.1, the standard deviations calculated are in good agreement with the measured ones. But, of course, in this case, the final droplet diameters are greatly underestimated.

Considering the large experimental uncertainty, the complexity of the phenomena involved, and the absence of literature dealing with gravity-induced coalescence in such a long column, deeper investigations will be needed to probe the origins of these discrepancies. Nevertheless, the results obtained are worthy of interest for the following stages of this study.

4.3.2. Heated spray

For these calculations, the same operating conditions as for the pure evaporation modelling have been used: i.e. flow rates of solute + water droplets following law 2 (i.e. closed configuration), but the spray velocities at the half-radius position were considered instead of the mean velocities. The same initial droplet size distributions as previously were used. A coalescence efficiency still equal to 0.39 was considered.

The mean particle diameters calculated at the column exit for the four flow rates are reported in Fig. 7, considering only pure evaporation (results logically identical with those of Section 3.2) and evaporation + coalescence. Thus, we can see that the effect of coalescence on the final particle diameter increases as the flow rate decreases: it is almost negligible for the highest flow rate (+2.5% on final diameter) whereas it is significant for the lowest flow rate (+10%). A longer time of evaporation for the lowest flow rate obviously promotes coalescence. The fact that the largest final droplet diameter is obtained for the highest flow rate is not due to coalescence but to the larger initial droplet mean diameter (see Fig. 6) and to the incompleteness of the evaporation process.

Fig. 8 reports the temporal evolutions of growth rates of the mean droplet radius (i.e. $R_0^{-1}(\mathrm{d}R/\mathrm{d}t)$) induced by coalescence

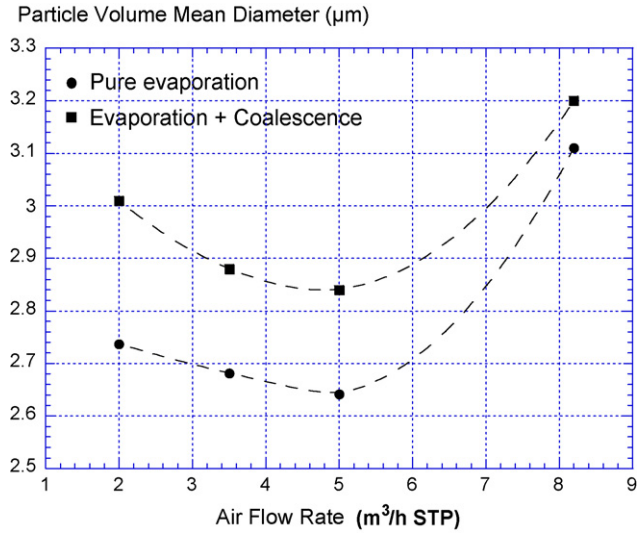

Fig. 7. Volume particle mean diameters calculated for several air flow rates/solution flow rates following law 2 considering only evaporation and evaporation + coalescence, heated spray.

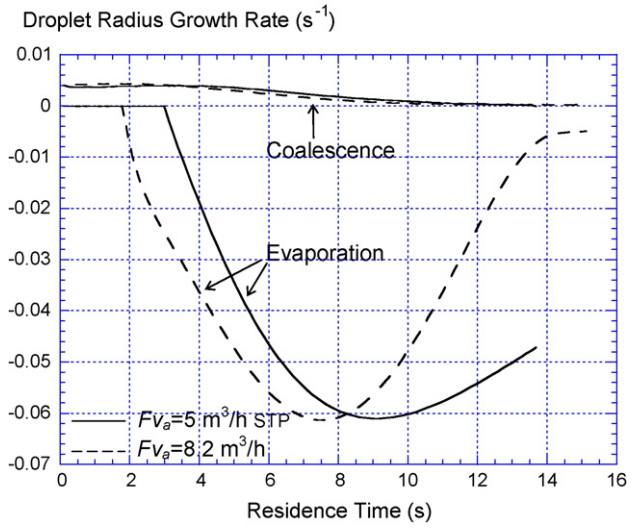

Fig. 8. Growth rates of droplet mean radius induced by coalescence/evaporation phenomena vs. residence time, for $Fv_a = 3.5$ and $8.2\ m^3\ h^{-1}$ STP.

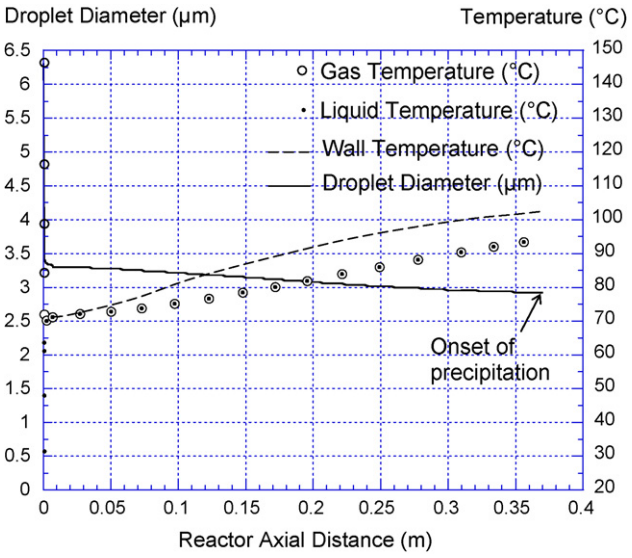

Fig. 9. Variation of the droplet radius, gas and liquid temperatures along the reactor axis for water + $Y(NO_3)_3$—$Fv_a = 5\ m^3\ h^{-1}$ STP, $Fv_w = 0.581\ h^{-1}$ STP, $d_0 = 5.2\ \mu m$.

on the one hand and by evaporation phenomena on the other, for the two highest air flow rates. The sum of the two contributions gives the total growth rate of the droplet radius, which is first positive since only coalescence occurs and then negative since the evaporation process predominates. Actually, coalescence is really significant only during the first half of the evaporation stage. The evaporation process is maximum around the middle of the heated zone, whereas the coalescence-driven growth rate is already half that calculated at the column inlet: this is not surprising since coalescence frequencies vary with R^2. Coalescence is negligible at the end of the evaporation stage. Broadly, coalescence plays a minor role in comparison with evaporation on the change occurring in droplet diameter.

Finally, the results of the calculations show that the best operating conditions to minimise the mean diameter of the formed particles are obtained with the third flow rate ($Fv_{a3} = 5\ m^3\ h^{-1}$ STP).

4.4. Global optimisation of the evaporation stage

The aim of this modelling study is to suggest ways to reduce coalescence and thus final particle diameters keeping high production rates of powder. This could be done by improving the features of the nebuliser so droplet size distributions would be narrower. Obviously, to generate droplet size distributions with smaller mean diameters would be also favourable, but would necessarily lower production rates. The unheated zone of the column could be also slightly shortened. Optimisation could finally act on some process parameters so as to reduce the total duration of the evaporation stage:

- increasing the walls temperature;
- injecting additional air (possibly preheated) at the bottom of the column, just after the generation of the spray;
- injecting a preheated flow of air directly in the nebuliser.

The first two suggestions would have the drawbacks of increasing the temperature gradients or inhomogeneities in the flow. The last suggestion seems a priori the most attractive.

For the third air flow rate ($Fv_{a3} = 5\ m^3\ h^{-1}$ STP) and the same processing conditions as previously, excepted the initial temperature of the air flow rate injected in the nebuliser, a modelling study was performed. It was assumed that the droplet size distribution generated by the preheated air flow is initially the same as that generated by cold air.

A quite interesting condition was obtained when injecting an air flow at a temperature of 140 °C. Evolutions of mean droplet diameter and of air and droplet temperatures calculated along the column axis are reported in Fig. 9. One millimetre (i.e. two-tenth of second) after the area of spray generation, heat transfer from air to droplets was already complete and liquid and gas temperatures of 71.5 °C. Obviously, during this first stage, the mean droplet diameter has decreased sharply and reached 3.3 µm. Then, the experimental thermal profile of Fig. 1 is considered for calculations (and reported in Fig. 9): the spray is now heated by the heating flux from the walls. The onset of precipitation is reached at a height of 0.37 m for a mean droplet diameter of 2.9 µm.

Note that the first stage of evaporation is so rapid that solute concentration gradients can appear inside droplets. All the same, any solute concentration gradient appearing during this stage has largely sufficient time to disappear during the second one.

From calculation, coalescence is completely insignificant for these operating conditions.

5. Conclusion

Spray pyrolysis is an efficient process to prepare micronic particles of europium-doped yttrium oxide Y_2O_3:Eu used for luminescent applications. However, the influence of the main

operating conditions was not well understood. Moreover, coalescence phenomena often occurred resulting in greater final particle diameters than expected and enlargement of particle size distributions.

To progress in understanding and optimising the process, a modelling study of the evaporation stage was performed at the scale of the column and of the individual droplets. Pure evaporation then both evaporation and coalescence phenomena were considered. Different processing conditions were tested on the basis of experimental data.

For the conditions simulated, it was demonstrated that the limiting step of the process is heat transfer from reactor walls to the air flow. As a consequence, the temperature of the liquid phase is always equal to that of the gas phase and droplet diameter and solute concentrations only depend on the local temperature. Thus, the onset of precipitation always occurs at the same temperature (here 95 °C).

A numerical approach based on physical models was developed to simulate gravity-induced coalescence. Conditions of pure coalescence and then of coupled evaporation/coalescence were simulated. As a general result for the conditions tested, coalescence plays a minor role, in comparison with evaporation, on the temporal evolution of droplet diameter. It appeared that the increase of the final droplet diameter due to coalescence is maximum for the lowest air flow rate reaching a value of 10%.

Finally, we considered the different ways to reduce coalescence without loss of production rates. The most attractive method a priori is to inject a preheated air flow directly in the nebuliser: the conditions used were found by calculation to be optimal, coalescence being completely insignificant.

Acknowledgements

We gratefully acknowledge Prof. J.P. Couderc for his valuable contribution and Dr. Nicolas Joffin for the experimental determinations and for helpful discussions. This work has been supported by the French Ministère de la Recherche (RNMP/POSUMIC).

Appendix A

Assuming that:

1. The transmission of momentum from droplets i to a droplet j is total during collision/coalescence events,
2. The density ρ_{liq} is locally the same for all the droplets. It is obviously the case for a spray of pure water droplets, it is also the case for a spray of solute + water droplets in our processing conditions since the compositions of all the droplets are locally the same (see Section 3.3),

the force $\mathbf{F}_{i\to j}$ resulting of the transmission of momentum from droplets i to a droplet j is given by:

$$\mathbf{F}_{i\to j} = \frac{v_{\text{gas}}}{v_j} f_{ij} m_{\text{d}_i} v_i \mathbf{e}_z = \frac{4}{3}\pi\rho_{\text{liq}} \frac{v_{\text{gas}}}{v_j} f_{ij} R_i^3 v_i \mathbf{e}_z \tag{A.1}$$

The drag force $\mathbf{F}_{\text{D},j}$ applied by the carrier gas on droplet j is given by [19,29]:

$$\mathbf{F}_{\text{D},j} = \tfrac{1}{2} C_{\text{D},j} \pi R_j^2 \rho_{\text{gas}} (v_{\text{gas}} - v_j)^2 \mathbf{e}_z \tag{A.2}$$

where $C_{\text{D},j}$ is the drag force coefficient. It can be estimated by the Stokes law for $Re_j < 1$:

$$C_{\text{D},j} = \frac{24}{Re_j} \tag{A.3}$$

or by the following relation for $2 < Re_j < 800$ [29]:

$$C_{\text{D},j} = \frac{14}{Re_j^{0.5}} \tag{A.4}$$

We will use the following relation a priori valid for $0.6 < Re < 3$ [29]:

$$C_{\text{D},j} = \frac{24}{Re_j}(1 + 0.13\, Re_j^{0.85}) \tag{A.5}$$

Actually, we verified from (A.3) and (A.4) that relation (A.5) gives a good estimation of the drag force coefficient for: $0.001 < Re_j < 40$, which is quite a sufficient range for our study. The particle Reynolds number Re_j is given by:

$$Re_j = \frac{2\rho_{\text{gas}} R_j (v_{\text{gas}} - v_j)}{\mu_{\text{gas}}} \tag{A.6}$$

The gravity force $\mathbf{P}_j$ is given by:

$$\mathbf{P}_j = -\tfrac{4}{3}\pi R_j^3 \rho_{\text{liq}} g \mathbf{e}_z \tag{A.7}$$

Then, the variation of the momentum versus time can be written:

$$\frac{\mathrm{d}\mathbf{p}_j \mathbf{e}_z}{\mathrm{d}t} = \frac{\mathrm{d}(m_{\text{d}_j}\mathbf{v}_j)}{\mathrm{d}t} = \frac{4}{3}\pi \left[R_j^3 v_j \frac{\mathrm{d}\rho_{\text{liq}}}{\mathrm{d}t} + \rho_{\text{liq}} \frac{\mathrm{d}(R_j^3 v_j)}{\mathrm{d}t} \right] \tag{A.8}$$

It can be easily shown by numerical applications that the first term in brackets of the previous expression is very insignificant with regard to the second one, therefore we can write:

$$\frac{\mathrm{d}\mathbf{p}_j \mathbf{e}_z}{\mathrm{d}t} = \frac{4}{3}\pi\rho_{\text{liq}} \frac{\mathrm{d}(R_j^3 v_j)}{\mathrm{d}t} \tag{A.9}$$

Thus, from (A.1), (A.2), (A.5)–(A.7) and (A.9), the equation of momentum conservation for a droplet j (22) can be written as:

$$\begin{aligned} \frac{\mathrm{d}(R_j^3 v_j)}{\mathrm{d}t} = {} & \frac{9}{2}\frac{\mu_{\text{gas}}}{\rho_{\text{liq}}} R_j (v_{\text{gas}} - v_i) \\ & \times \left[1 + 0.13 \left(\frac{2\rho_{\text{gas}} R_j}{\mu_{\text{gas}}} \right)^{0.85} (v_{\text{gas}} - v_i)^{0.85} \right] \\ & + \frac{v_{\text{gas}}}{v_j} f_{ij} R_i^3 v_i - g R_j^3 \end{aligned} \tag{A.10}$$

Writing now: $Z_j = R_j^3 v_j$, Eq. (A.10) becomes:

$$\frac{\partial Z_j}{\partial t} = \frac{9}{2}\frac{\mu_{\text{gas}}}{\rho_{\text{liq}}} R_j \left(v_{\text{gas}} - \frac{Z_j}{R_j^3} \right) \times \left[1 + 0.13 \left(\frac{2\rho_{\text{gas}} R_j}{\mu_{\text{gas}}} \right)^{0.85} \left(v_{\text{gas}} - \frac{Z_j}{R_j^3} \right)^{0.85} \right] + v_{\text{gas}} R_j^3 f_{ij} \frac{Z_i}{Z_j} - g R_j^3 \quad \text{(A.11)}$$

Generalizing this equation to a spray composed of n populations of droplets with different radii, the following equation is obtained:

$$\frac{\mathrm{d}Z_i}{\mathrm{d}t} = \frac{9}{2}\frac{\mu_{\text{gas}}}{\rho_{\text{liq}}} R_i \left(v_{\text{gas}} - \frac{Z_i}{R_i^3} \right) \times \left[1 + 0.13 \left(\frac{2\rho_{\text{gas}} R_i}{\mu_{\text{gas}}} \right)^{0.85} \left(v_{\text{gas}} - \frac{Z_i}{R_i^3} \right)^{0.85} \right] + \frac{v_{\text{gas}} R_i^3}{Z_i} \sum_{j=1}^{i-1} f_{ji} Z_j - g R_i^3 \quad \text{(A.12)}$$

If $\mathbf{F}_{i\to j}$ is ignored, relation (23) is obtained and calculations show that the terminal settling velocity $V_{\text{TS}j}$ can be very well fitted by the following relation in our range of processing conditions:

$$V_{\text{TS}\,j} = a + b\cos(cR_j + d) \quad \text{(A.13)}$$

with: $a = 0.29082902$, $b = 0.29081879$, $c = 28228.518$ and $d = 3.1407123$.

Appendix B. Nomenclature

a_{w}	water activity
C_{D}	drag force coefficient
Cp	specific heat ($\text{J kg}^{-1}\,\text{K}^{-1}$)
$Cp_{\text{w}}^{\text{vap}}$	specific heat of water vapour ($\text{J kg}^{-1}\,\text{K}^{-1}$)
d	droplet diameter (m)
D_{v}	binary diffusion coefficient of air/water vapour ($\text{m}^2\,\text{s}^{-1}$)
f_{ij}	coalescence frequency of droplets i with a droplet j (s^{-1})
$f(T)$	function defined by relation (15)
F	mass flow rate (kg s^{-1})
$\mathbf{F}_{\text{D}}$	drag force (N)
$\mathbf{F}_{i\to j}$	force resulting from the transmission of momentum from droplets i to a droplet j (N)
F_{ij}	coalescence frequency of droplets i with droplets j (s^{-1})
Fv	volume flow rate ($\text{m}^3\,\text{h}^{-1}$ STP)
g	universal constant of gravitation (m s^{-2})
h_{vap}	vapourisation enthalpy of water (J kg^{-1})
m_{d}	droplet mass (kg)
m_{s}	mass of solute in droplet (kg)
M	molar weight (kg mol^{-1})
n	droplet number density (m^{-3})
$\mathbf{p}$	momentum of a droplet (kg m s^{-2})
$\mathbf{P}$	gravity force (N)
P_{sat}	saturation pressure of water vapour in air (Pa)
P_{vap}	partial pressure of water vapour in air (Pa)
P_0	ambient pressure (Pa)
q	heat flux density at the inner column walls (W m^{-2})
R	droplet radius (m)
$R^{\dagger}$	virtual droplet radius (m)
R_{c}	column radius (m)
R_{p}	droplet radius at the onset of precipitation (m)
Re	particle Reynolds number
S	solubility (g/100 g of water)
t	time (s)
T	temperature (K)
T_{spray}	temperature of the spray (K)
T_{wall}	inner wall temperature (K)
v	axial velocity (m s^{-1})
w_{a}, $w_{\text{w}}^{\text{vap}}$	mass fractions of air/water vapour in gas
$w_{\text{s}}^{\text{liq}}$	mass fractions of $Y(NO_3)_3$ in droplet
$w_{\text{w}}^{\text{cryst}}$	mass fraction of water present as hydrates of yttrium nitrate in droplet
$w_{\text{w}}^{\text{liq}}$	mass fraction of liquid water in droplet
X, Y	relative mass fractions defined by relation (2)
X_{sat}	X at the solubility limit
Y_{int}	Y defined by relation (7)
z	axial coordinate (m)

Greek symbols

ε_{ij}	coalescence efficiency
κ	overall heat transfer coefficient ($\text{W m}^{-2}\,\text{K}^{-1}$)
λ	thermal conductivity ($\text{W m}^{-1}\,\text{K}^{-1}$)
μ	dynamic viscosity (Pa s)
ρ	density (kg m^{-3})

Subscripts

0	initial value
a	air
d	droplet
gas	gas
i, j	droplet i or j
int	at the gas/liquid interface
liq	liquid
s	solute
sat	in the saturated solution (i.e. at the solubility limit)
w	water

References

[1] A. Gurav, T. Kodas, T. Pluym, Y. Xiong, Aerosol processing of materials, Aerosol Sci. Technol. 19 (1993) 411–452.

[2] S.E. Pratsinis, S. Vemury, Particle formation in gases, Powder Technol. 88 (1996) 267–273.

[3] N. Joffin, Synthèse par pyrolyse d'aérosol et caractérisation de luminophores: Y_2O_3:Eu et Zn_2SiO_4:Mn pour application dans les panneaux à plasma, Ph.D. Thesis, Institut National Polytechnique Toulouse, France, 2004.

[4] C.R. Ronda, Recent achievements in research on phosphors for lamps and displays, J. Lumin. 72–74 (1997) 49–54.

[5] Y.C. Kang, S.B. Park, I.W. Lenggoro, K. Okuyama, Preparation of non-aggregated Y_2O_3:Eu phosphor particles by spray pyrolysis method, J. Mater. Res. 14-6 (1999) 2611–2615.
[6] N. Reuge, N. Joffin, J. Dexpert-Ghys, M. Verelst, H. Dexpert, B. Caussat, Y_2O_3 micronic particles synthesised by spray pyrolysis: process modelling and considerations about the particle hollowness, J. Mater. Process. Technol., submitted for publication.
[7] G.V. Jayanthi, S.C. Zhang, G.L. Messing, Modeling of solid particle formation during solution aerosol thermolysis—the evaporation stage, Aerosol Sci. Technol. 19 (1993) 478–490.
[8] H.-F. Yu, Simulation of spray pyrolysis for ceramic powder preparation, Particulate Sci. Technol. 13 (1995) 149–167.
[9] H.-F. Yu, W.-H. Liao, Evaporation of solution droplets in spray pyrolysis, Int. J. Heat Mass Transfer 41 (1998) 993–1001.
[10] Y. Xiong, T.T. Kodas, Droplet evaporation and solute precipitation during spray pyrolysis, J. Aerosol Sci. 24-7 (1993) 893–908.
[11] S. Sommerfeld, Analysis of isothermal and evaporating turbulent sprays by phase-Doppler anemometry and numerical calculations, Int. J. Heat Fluid Flow 19 (1998) 173–186.
[12] F. Laurent, M. Massot, P. Villedieu, Eulerian multi-fluid modeling for the numerical simulation of coalescence in polydisperse dense liquid sprays, J. Comput. Phys. 194 (2004) 505–543.
[13] S. Khosid, On the solution of population balance equations for multi-size aerosol cloud undergoing simultaneous evaporation and coalescence, Aerosol Sci. 33 (2002) 533–551.
[14] F. Anidjar, Y. Tambour, J.B. Greenberg, Mass exchange between droplets during head-on collisions of multisize sprays, Int. J. Heat Mass Transfer 38-18 (1995) 3369–3383.
[15] P.J. O'Rourke, F.V. Bracco, Modelling of drop interactions in thick sprays and comparison with experiment, in: Stratified Charge Auto Engines Conference, I. Mech E., London, 1980, pp. 101–116.
[16] J.B. Greenberg, I. Silverman, Y. Tambour, On the origin of spray sectional conservation equations, Combust. Flame 93 (1993) 90–96.
[17] S.H. Lee, G.H. Ko, H.S. Ryou, A numerical study on the spray-to-spray impingement system, KSME Int. J. 16-2 (2002) 235–245.
[18] S.W. Lyons, J. Ortega, L.M. Wang, T.T. Kodas, Multicomponent ceramic powder generation by spray pyrolysis, Mater. Res. Soc. Symp. Proc. 271 (1992) 907–917.
[19] W.C. Hinds, Aerosol Technology, John Wiley & Sons, New York, 1982.
[20] J.A. Rard, Solubility determinations by the isopiestic method and application to aqueous lanthanide nitrates at 25 °C, J. Solut. Chem. 14-7 (1985) 457–471.
[21] R.C. Reid, J.M. Prausnitz, T.K. Sherwood, The Properties of Gases and Liquids, third ed., McGraw-Hill, New York, 1977.
[22] J.A. Dean, Lange's Handbook of Chemistry, 13th ed., McGraw-Hill, New York, 1985.
[23] R. Bouchet, R. Tenu, J.J. Counioux, Etude expérimentale et modélisation des équilibres solide-liquide des binaires eau-nitrate d'yttrium, de baryum, de cuivre. Partie 1. Les binaires H_2O-$Ba(NO_3)_2$ et H_2O-$Y(NO_3)_3$, Thermochim. Acta 241 (1994) 229–246.
[24] W.E. Ranz, W.R. Marshall Jr., Evaporation from drops: Part I and Part II, Chem. Eng. Prog. 48 (141-46) (1952) 173–180.
[25] http://www.pdesolutions.com
[26] http://www.scilab.org
[27] R.B. Bird, W.E. Stewart, E.N. Lightfoot, Transport Phenomena, John Wiley & Sons, New York, 1960.
[28] E.U. Schlünder, Temperature und masseänderung verdunstander tropfen aus reinen flüssigkeiten und wässrigen salzlosungen, Int. J. Heat Mass Transfer 7 (1964) 49–73.
[29] A. Renoux, D. Boulaud, Les aérosols—Physique et métrologie, Lavoisier, Paris, 1998.
[30] A. Karnis, H.L. Goldsmith, S.G. Mason, The kinetics of flowing dispersions. I. Concentrated suspensions of rigid particles, J. Colloid Interface Sci. 22 (1966) 531–553.
[31] W. Stumm, J. Morgan, Aquatic Chemistry, second ed., Wiley Interscience, New York, 1981.
[32] M.Z. Jacobson, Fundamentals of Atmospheric Modeling, second ed., Cambridge University Press, 2005.
[33] X. Zhang, R.H. Davis, The rate of collision due to Brownian or gravitational motion of small drops, J. Fluid Mech. 230 (1991) 479–504.
[34] H. Wang, R.H. Davis, Collective effects of gravitational and Brownian coalescence on droplet growth, J. Colloid Interface Sci. 178 (1996) 47–52.
[35] R.H. Davis, The rate of coagulation of a dilute polydisperse system of sedimenting spheres, J. Fluid Mech. 145 (1984) 179.
[36] M. Barbes Le Borgne, Etude expérimentale et théorique de la coagulation des aérosols liquides, Ph.D. Thesis, Paris XII, France, 1987.
[37] C.S. Wen, The Fundamentals of Aerosol Dynamics, World Scientific Publishing Co., River Edge, NJ, 1996.